Targeting glioma stem cells through combined BMI1 and EZH2 inhibition

Xun Jin[1–3] , Leo J Y Kim[1,4–6], Qiulian Wu[1,6], Lisa C Wallace[1], Briana C Prager[1,4–7], Tanwarat Sanvoranart[1], Ryan C Gimple[1,4–6], Xiuxing Wang[1,6], Stephen C Mack[1,8] , Tyler E Miller[1,4,5], Ping Huang[1], Claudia L Valentim[1], Qi-gang Zhou[1], Jill S Barnholtz-Sloan[9], Shideng Bao[1,7,9], Andrew E Sloan[9,10] & Jeremy N Rich[1,6,7,9]

Glioblastomas are lethal cancers defined by angiogenesis and pseudopalisading necrosis. Here, we demonstrate that these histological features are associated with distinct transcriptional programs, with vascular regions showing a proneural profile, and hypoxic regions showing a mesenchymal pattern. As these regions harbor glioma stem cells (GSCs), we investigated the epigenetic regulation of these two niches. Proneural, perivascular GSCs activated EZH2, whereas mesenchymal GSCs in hypoxic regions expressed BMI1 protein, which promoted cellular survival under stress due to downregulation of the E3 ligase RNF144A. Using both genetic and pharmacologic inhibition, we found that proneural GSCs are preferentially sensitive to EZH2 disruption, whereas mesenchymal GSCs are more sensitive to BMI1 inhibition. Given that glioblastomas contain both proneural and mesenchymal GSCs, combined EZH2 and BMI1 targeting proved more effective than either agent alone both in culture and *in vivo*, suggesting that strategies that simultaneously target multiple epigenetic regulators within glioblastomas may be effective in overcoming therapy resistance caused by intratumoral heterogeneity.

Glioblastoma is the most prevalent and lethal primary brain tumor, with current therapies offering only palliation[1]. Glioblastomas represent one of the most rigorously characterized solid cancers, yet delineation of molecular lesions has not translated into effective targeted therapeutics. Glioblastomas display remarkable heterogeneity, both between tumors (intertumoral heterogeneity) and within tumors (intratumoral and cellular heterogeneity), indicating a molecular and cellular complexity that is unlikely to respond to targeting of single molecular pathways. Glioblastomas contain stem cell–like tumor-initiating cells called GSCs (also known as cancer stem cells)[2,3]. Whereas the definition and origin of GSCs are unresolved, their significance has been supported by observations that they promote resistance to conventional therapies, invasion into normal brain and angiogenesis[4–6]. GSCs are not uniformly distributed within tumors but rather are enriched in perivascular and hypoxic niches, suggesting that GSCs critically interact with their microenvironment[6–8]. Indeed, microenvironmental stressors, such as hypoxia, acid and nutrient restriction, promote GSC maintenance[7,9,10].

Global transcript profiling and DNA methylation analyses from bulk adult glioblastoma samples have categorized glioblastoma into several distinct subtypes: glioma CpG island methylator phenotype (G-CIMP), which is associated with mutations in the genes encoding isocitrate dehydrogenases 1 and 2 (*IDH1* and *IDH2*); non-G-CIMP proneural; classical or proliferative; and mesenchymal[11]. Genomic profiling has not been able to guide precision medicine efforts for glioblastoma[12], possibly because the tumors comprise cell populations with divergent subtype-specific gene expression[13,14]. Glioblastoma transcriptional groups, including a tendency toward proneural-to-mesenchymal transition after cytotoxic therapy, are plastic[15,16]. Nevertheless, tumor cells grown under stem cell conditions recapitulate the dominant subtype of the parental tumor, suggesting retention of a cell-intrinsic biology[17,18]. We hypothesized that the heterogeneous distribution of GSCs suggests that they reside in different niches, requiring differential therapeutic targeting of different subsets in the context of their specific niches.

RESULTS

As bulk tumors contain cells from different subgroups[13], we profiled expression patterns within specific tumor microenvironments by image-guided multiregional glioblastoma sampling (**Fig. 1a**). Tumor cells from the enhancing region (ER), defined by disruption of the blood–brain barrier at areas of angiogenesis, showed high expression of proneural genes, whereas the necrotic region (NR; hypoxic) show high expression of mesenchymal genes (**Fig. 1b**). An intermediate

tumor region (enhanced margin, EM) displayed a mixed transcriptional signature comprising classical and proneural gene expression signatures (**Fig. 1b**). These findings were validated in two other multiregional patient biopsies with glioblastoma subtype gene signatures (**Supplementary Fig. 1**). GSCs displayed regional variation, measured by immunofluorescence of each region using the proneural GSC markers SOX2 and OLIG2 and the mesenchymal GSC markers CD44 and YKL40 (refs. 16,19). GSCs in the ER were exclusively SOX2^{+} and OLIG2^{+}, whereas NR GSCs were exclusively CD44^{+} and YKL40^{+}, indicating segregation of proneural and mesenchymal GSC markers (**Fig. 1c**). Gene expression profiling for vascular and hypoxic markers confirmed that proneural-enriched cells were associated with vascular regions, and mesenchymal cells, with hypoxia (**Fig. 1d**). Immunofluorescence staining using von Willebrand factor (vWF) for vessels and carbonic anhydrase 9 (CA9) for hypoxia confirmed the regional variance of vascularity and hypoxia (**Fig. 1e**). To validate our observations in a larger tumor cohort, we interrogated the Ivy Glioblastoma Atlas Project (Ivy GAP) database, which contains data from 42 glioblastomas regionally microdissected with RNA-seq (http://glioblastoma.alleninstitute.org/). Confirming our findings from the MRI-guided biopsy results, the leading edge and infiltrating tumor regions expressed a proneural signature, whereas perinecrotic and microvascular proliferative regions expressed a mesenchymal signature (**Fig. 1f**–**h**).

Next, we constructed microenvironment-related gene signatures based on microarray data from vascular sources (human umbilical vein endothelial cells (HUVEC) and human microvascular endothelial cells (HMVEC)) and analyses comparing glioblastoma hypoxia to normoxia[20,21] (**Supplementary Figs. 2a,b** and **3a,b**). Selected signatures and genes were analyzed in glioblastoma samples and the Ivy GAP database (**Supplementary Figs. 2c,f,i** and **3c,f**). In The Cancer Genome Atlas (TCGA) low-grade glioma–glioblastoma database, both vascular signatures and hypoxia were expressed in glioblastoma (**Supplementary Figs. 2d,g** and **3d**) and associated with tumor histology, grade and defining molecular features (**Supplementary Fig. 4a**). Proneural glioblastomas expressed markers of mature vessels, whereas mesenchymal glioblastomas expressed markers for microvasculature and hypoxia[22,23] (**Supplementary Figs. 2e,h** and **3e**). Both vascular signatures and hypoxia were anticorrelated with patient survival (**Supplementary Figs. 2j,k** and **3g**). Patients with both vascularity and hypoxic expression patterns fared the worst (**Supplementary Fig. 4b**), supporting microvascular and hypoxic microenvironments as major predictors of unfavorable glioblastoma patient survival[24,25]. Our multiregional patient biopsy samples validated these *in silico* observations, demonstrating that the regional variation in transcriptional signatures correlated with vascular and hypoxic features (**Supplementary Fig. 4c,d**).

Regional transcriptional variation may reflect differences in chromatin regulation. Polycomb repressive complexes (PRCs) comprise major chromatin modifiers of epigenetic regulation of global gene expression. PRC1 and PRC2 regulate chromatin compaction through specific histone modifications: PRC2 first binds to chromatin and its catalytic subunit, EZH2, trimethylates histone H3 at residue K27 (H3K27me3). H3K27me3 is then recognized by PRC1, which contains BMI1, then monoubiquitination of histone 2A on K119 (H2AK119Ub) causes chromatin compaction and pausing of RNA polymerase II. However, recent evidence suggests that PRC1 can also silence gene expression through a noncanonical, H3K27me3-independent mechanism[26]. Given this background, we investigated PRC1 and PRC2 activity with H2AK119Ub and H3K27me3 staining

in multiregional patient biopsy samples, observing dichotomous distribution of cells positive for H2AK119Ub and H3K27me3 in hypoxic (necrotic) and vascular (enhancing) regions, respectively (**Fig. 2a** and **Supplementary Fig. 5a**). As the GSC markers CD133 and CD44 may be specific for glioblastoma subgroup[16], we employed another GSC marker, CD15 (also known as SSEA1)[27], which was less specific but more sensitive than CD133 (data not shown). CD15^{+} cells in different regions expressed H2AK119Ub or H3K27me3 and displayed functional characteristics of GSCs (**Fig. 2a** and **Supplementary Fig. 5a**–**c**). Using image-guided biopsies from two glioblastomas, we interrogated genome-wide distribution of chromatin marks from PRC1 (H2AK119Ub)[28] or PRC2 (H3K27me3) in CD15^{+} GSCs from enhancing and necrotic regions using chromatin immunoprecipitation followed by deep sequencing (ChIP-seq). To determine region-specific peaks, we analyzed overlapping peaks in both samples and identified peaks that were both unique to a particular anatomic region and were shared between the samples (**Fig. 2b**). Annotation of region-specific genes marked by H3K27me3 or H2AK119Ub in the same anatomic region from both patients revealed that more than 80% of region-specific target genes displayed differential H3K27me3 or H2AK119Ub marks (**Fig. 2c** and **Supplementary Table 1**), indicating distinct PRC function in GSCs residing in different regions. While intertumoral variation was substantial, shared regions converged on important gene targets. H3K27me3, generally associated with inhibition of transcription, marked neuronal and cellular development targets in both the ER and NR, albeit without substantial overlap in gene identity, with EZH2, SUZ12 and H3K27me3 targets most significantly marked by H3K27me3 in the ER (**Fig. 2d** and **Supplementary Table 1**). In contrast, H2AK119Ub marked very different targets in the ER and NR, with H2AK119Ub in CD15^{+} GSCs from the hypoxic regions marking genes strongly associated with mesenchymal signaling pathways, such as those encoding transforming growth factor-β (TGF-β), nuclear factor-κB (NF-κB) and WNT (**Fig. 2d** and **Supplementary Table 1**), indicating probable microenvironment-specific functions of PRC2 and PRC1. Furthermore, tumors with proneural signatures showed enrichment of an EZH2 activation signature (containing 41 putative targets or partners of EZH2)[29] (**Fig. 2e** and **Supplementary Fig. 6g**), whereas tumors with mesenchymal transcriptional profiles showed enrichment of a BMI1 activation signature (containing 341 genes downregulated upon BMI1 knockdown)[30] (**Fig. 2f** and **Supplementary Fig. 7g**). Using a glioblastoma tumor microarray, we confirmed the correlation of high EZH2 protein levels with high expression of OLIG2, a proneural marker, and high BMI1 protein levels with high expression of CD44, a mesenchymal marker (**Fig. 3a**).

To assess PRC contribution to microenvironment-specific distribution of glioblastoma subtypes, we correlated EZH2, BMI1 and microenvironment-related signatures. The EZH2 activation signature positively correlated with proneural and mature vascular signature but negatively correlated with mesenchymal and classical microenvironment signatures (**Supplementary Figs. 6f** and **8b,c**), implicating EZH2 function in tumor neovascular regions[31]. Conversely, a BMI1 activation signature correlated positively with mesenchymal or classical microenvironment signatures and negatively with a proneural microenvironment signature (**Supplementary Figs. 7f** and **8b,c**). EZH2 and BMI1 expression or activation signatures were associated with poor patient prognosis, but the worst prognosis was associated with high expression of both proteins or signatures (**Fig. 3b** and **Supplementary Figs. 6e,h,i, 7e,h** and **8a,d**), suggesting that combined PRC1–PRC2 activation portends greater tumor malignancy.
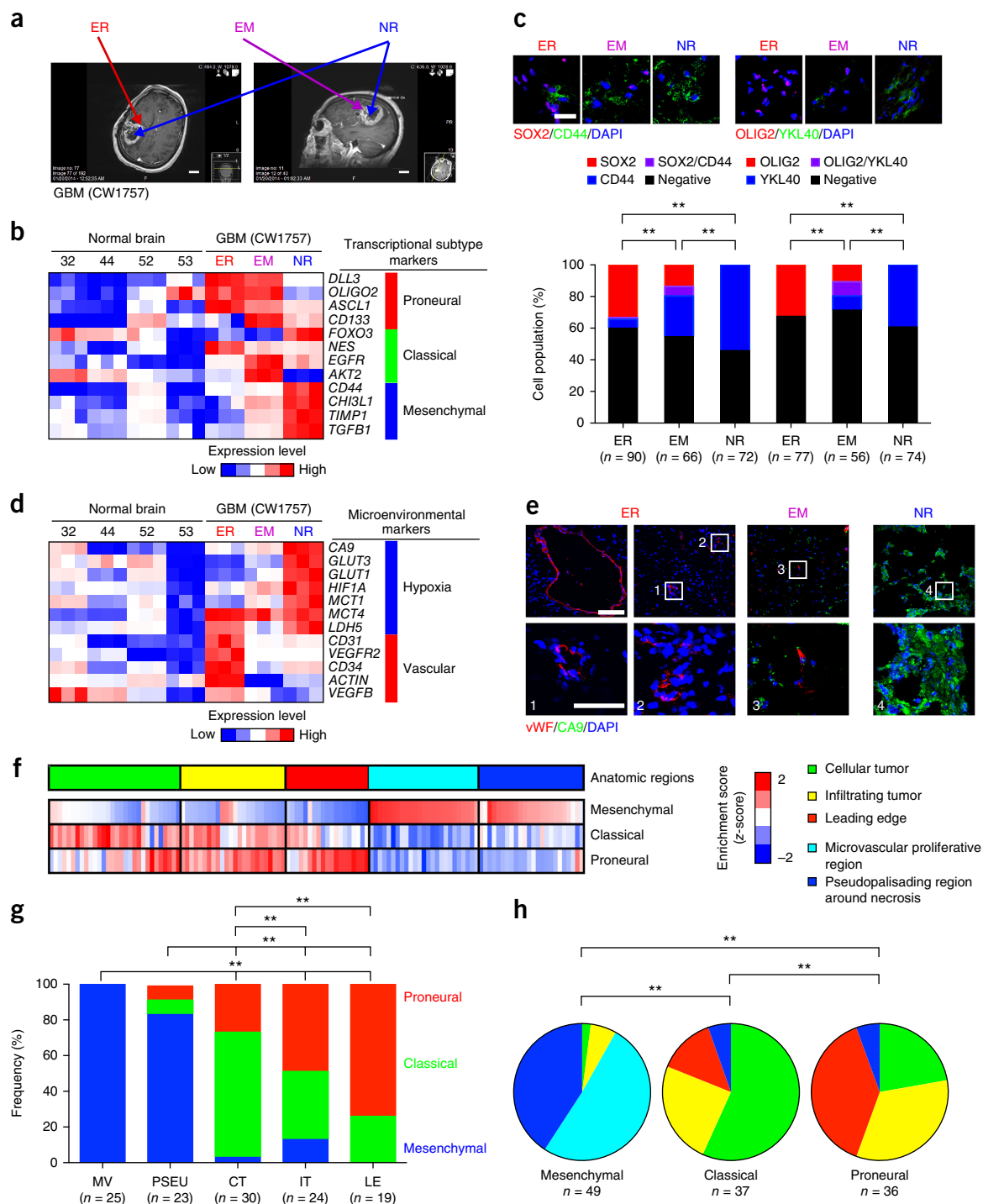
Figure 1 Anatomical distribution of transcriptional profiles in glioblastoma. (**a**) T1-weighted MRI images of multiregional glioblastoma sampling process (representative of four patients) for qPCR and immunofluorescence analysis. Scale bars, 2 cm. (**b**) A heat map of molecular subtype marker expression in three multiregional glioblastoma samples and four nonmalignant human brain samples. z-scores were calculated from qPCR ΔC_t values. (**c**) Immunofluorescence images (top, representative of 10 fields for each region) and quantification (bottom) of SOX2 (red), CD44 (green), OLIG2 (red) and YKL40 (green) expression in multiregional glioblastoma samples Scale bar, 25 μm. **$P < 0.001$, χ^2 test. (**d**) Heat map showing mRNA expression of markers of hypoxia (*CA9*, *GLUT3*, *GLUT1*, *HIF1A*, *MCT1*, *MCT4* and *LDH5*) and vascular specimen (*CD31*, *VEGFR2*, *CD34*, *ACTIN* and *VEGFB*) in three multiregional glioblastoma samples and four nonmalignant human brain samples. z-scores were calculated from change in qPCR ΔC_t values. (**e**) Immunofluorescence images (representative of three fields for each region) showing vWF+ (red) and CA9+ (green) locations in multiregional glioblastoma samples. Boxes and numbers (top) indicate areas shown in higher magnification (bottom). Scale bars 25 μm (top) or 10 μm (bottom). (**f**) Heat map showing z-scores of each glioblastoma subtype signature, normalized within each patient sample set determined via single-sample gene-set enrichment analysis (ssGSEA) for each RNA sample in the Anatomic Structure Study data set (RNA sample $n = 122$; patient $n = 10$) from the Ivy GAP database. The corresponding histological feature for each RNA sample is labeled (top). (**g,h**) χ^2 test of glioblastoma histological feature distributions among transcriptional profiles (**g**) and molecular subtype distribution among histological structures (**h**). **$P < 0.001$.
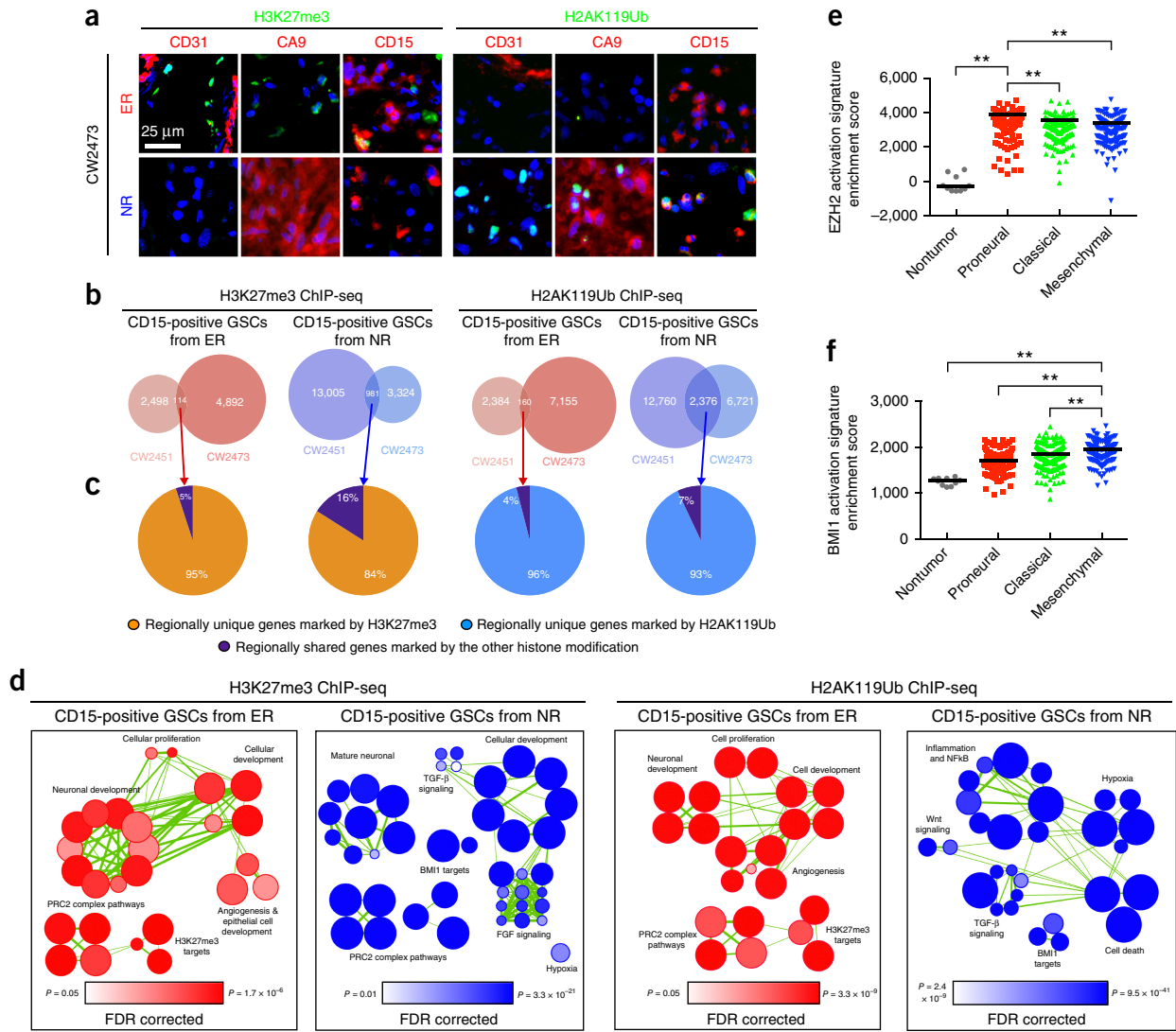
Figure 2 Epigenetic GSC signatures in multiregional primary specimens. (**a**) Immunofluorescence staining for CD31 (red), CA9 (red), CD15 (red), H3K27me3 (green) and H2AK119Ub (green) in multiregional glioblastoma samples. Scale bar, 25 μm. (**b**) Overlap in region-specific H3K27me3 or H2AK119Ub binding genes in CD15+ cells derived from primary glioblastoma samples (CW2451 and CW2473). Venn diagrams show overlaps between region specific peaks derived from H3K27me3 or H2AK119Ub ChIP-seq experiments on two primary glioblastoma specimens. (**c**) Fraction of region-specific peaks shown in **b** that are regionally unique annotated genes marked by H3K27me3 (orange) or H2AK119Ub (blue) and are common between enhancing or necrotic regions from both patients. Purple, the fraction of region-specific peaks shared by both patients within the same anatomic region and also called in the other histone modification ChIP-seq. (**d**) Bubble plots showing gene signatures enriched in the overlapping region-specific peaks shown in **b**. (**e**,**f**) Enrichment levels of EZH2 (**e**) or BMI1 (**f**) activation signatures in transcriptional subgroups from the TCGA glioblastoma data set ($n = 10$, nontumor; $n = 161$, proneural; $n = 209$, classical; $n = 167$, mesenchymal). Black bars indicate median values. **$P < 0.01$; one-way ANOVA with Tukey's method for multiple comparisons.

As both EZH2 and BMI1 regulate GSCs, we investigated BMI1 and EZH2 expression in several validated proneural and mesenchymal GSC and neural progenitor cell models. BMI1 and H2AK119Ub were markedly increased in CD44+ and YKL40+ mesenchymal GSCs, whereas EZH2 and H3K27me3 were associated with OLIG2+ and SOX2+ proneural GSCs (**Fig. 3c**). RNA-seq data from 19 patient-derived GSC models that we generated confirmed that *EZH2* mRNA and activity signatures correlated with a proneural signature, whereas BMI1 activation, but not *BMI1* mRNA, correlated with mesenchymal GSCs (**Supplementary Fig. 9**), indicating that BMI1 and EZH2 signaling pathways were activated in different GSC subtypes.

EZH2 mRNA expression levels correlated with the EZH2 activation signature and the proneural subtype and microenvironment in

TCGA tumor samples (**Supplementary Fig. 6**), but we were surprised to find that *BMI1* mRNA expression did not correlate with a BMI1 activation signature or the mesenchymal subtype or microenvironment signature (**Supplementary Fig. 7**), suggesting that EZH2 is regulated at the transcriptional level but BMI1 is regulated post-transcriptionally. Inhibiting translation with cycloheximide treatment showed that BMI1 protein levels were unchanged in mesenchymal GSCs but markedly reduced in proneural GSCs (**Supplementary Fig. 10a**). Conversely, polyubiquitinated BMI1 was strongly increased in proneural GSCs after treatment with the proteasome inhibitor lacta-cystin but weakly accumulated in mesenchymal GSCs under the same conditions (**Fig. 3d**), suggesting that ubiquitin-mediated proteolysis maintains BMI1 protein stability in GSCs of different subtypes.
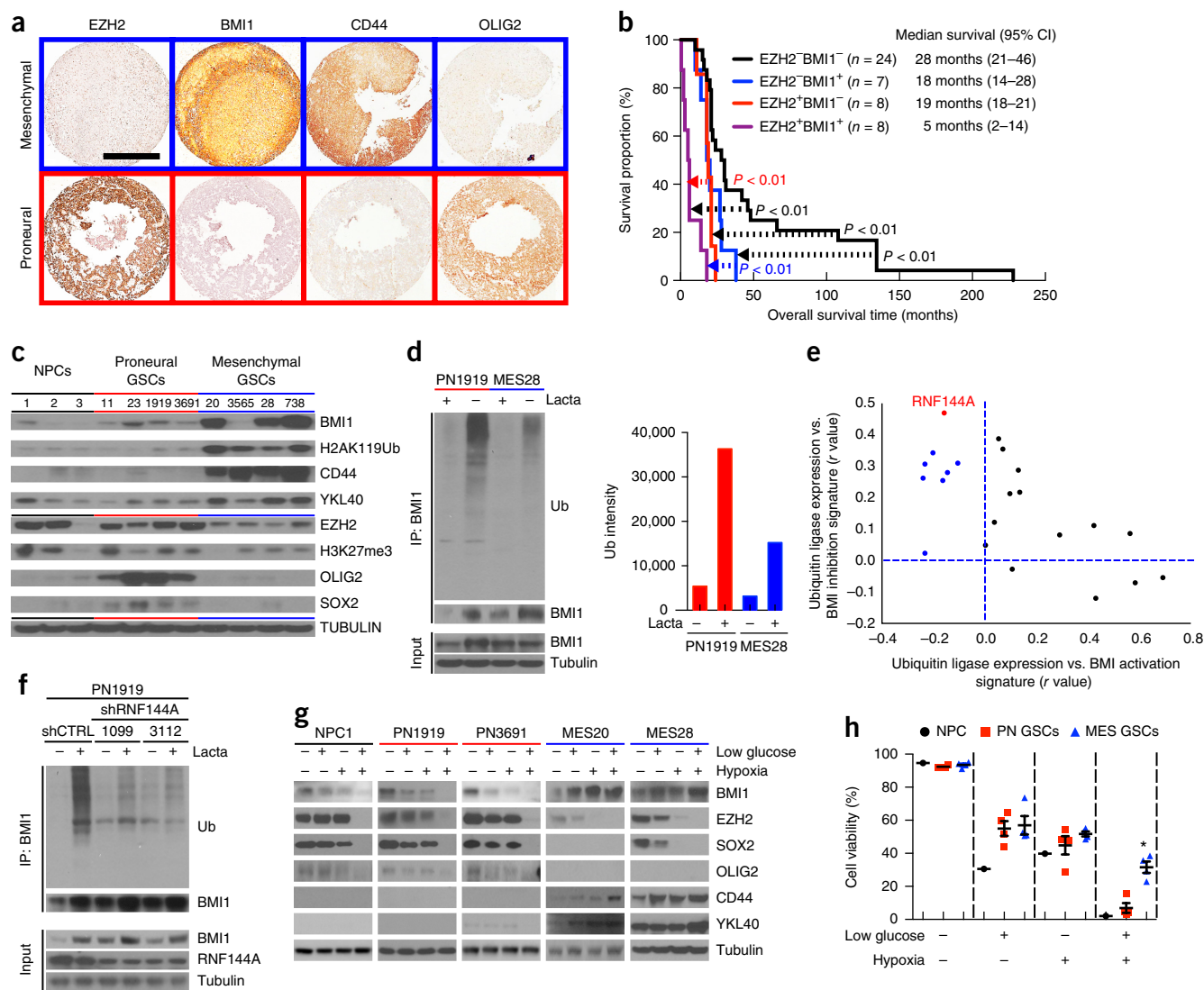
Figure 3 Differential PRC function in glioblastoma subgroups. (**a**) Representative images of glioblastoma tissue microarray samples (n = 96) showing the expression of EZH2, BMI1, CD44 and OLIG2. Scale bar, 500 μm. (**b**) Kaplan–Meier curves of patient survival stratified by EZH2 and BMI1 expression level from a glioblastoma tissue microarray (n = 24, EZH2−BMI1−; n = 7, EZH2−BMI1+; n = 8, EZH2+BMI1−; n = 8 EZH2+BMI1+). P values were determined by log-rank test. (**c**) Immunoblot analysis of BMI1, H2K119Ub, EZH2, H3K27me3 and marker expression in lysates from mesenchymal (CD44 and YKL40) and proneural (OLIG2 and SOX2) glioblastoma. Numbers (top) indicate sample ID. NPC, neural progenitor cell. All full-length immunoblots for data presented above are available in **Supplementary Figure 22**. (**d**) Left, immunoprecipitation (IP) and immunoblot (IB) analysis of BMI1 polyubiquitination in proneural (PN1919) and mesenchymal (MES28) cells in the presence or absence of lactacystin (lacta) treatment (5 h, 10 μM). Right, quantification of BMI1 polyubiquitination by ImageJ. Data are normalized by input loading controls. Ub, ubiquitin. (**e**) Rank-ordered list of r values between ubiquitin ligases and BMI1 activation or inhibition signatures in TCGA glioblastoma samples. (**f**) BMI1 polyubiquitination by RNF144A in PN1919 cells after transduction with shRNA control (shCTRL) or shRNF144A (shRNF144A-1099 and shRNF144A-3112) examined by BMI1- or ubiquitin-specific immunoprecipitation and immunoblotting in the presence or absence of lactacystin treatment as in **d**. BMI1, RNF144A and tubulin were analyzed by immunoblot in the input (whole-cell lysates). (**g**) Levels of RNF144A, BMI1, EZH2, CD44, YKL40, OLIG2 and SOX2 measured by immunoblot in neural progenitor cells (NPC1), proneural GSCs (PN1919 and PN3691) and mesenchymal GSCs (MES20 and MES28) grown under baseline conditions or in low-glucose and/or hypoxic conditions. (**h**) Viability NPC1 cells, proneural GSCs (PN11, PN23, PN1919 and PN3691) and mesenchymal GSCs (MES20, MES28, MES3565 and MES738) determined under baseline conditions or in low-glucose and/or hypoxic conditions. Data are as mean ± s.e.m. *P < 0.05, Wilcoxon and Mann–Whitney t-test.

On the basis of the apparent region-specific BMI1 proteosomal degradation, we interrogated the TCGA glioblastoma database for ubiquitin-related genes whose expression correlated inversely with BMI1 activation. Among 254 genes associated with ubiquitination, 22 were differentially expressed by proneural and mesenchymal glioblastomas (**Supplementary Fig. 10b**). To link these genes to BMI1 activity, we plotted r values for the 22 genes against two

BMI1-related signatures (**Fig. 3e**). The highest r value negatively associated with BMI1 activation was associated with the ring finger, RNF144A, which was previously described as an E3 ligase for DNA-dependent protein kinase, catalytic subunit DNA-PKcs[32]. Supporting its potential role as a BMI1 E3 ligase, RNF144A expression negatively correlated with BMI1 activation and positively correlated with a BMI1 inhibition signature (**Fig. 3e**). The results from ChIP-seq for
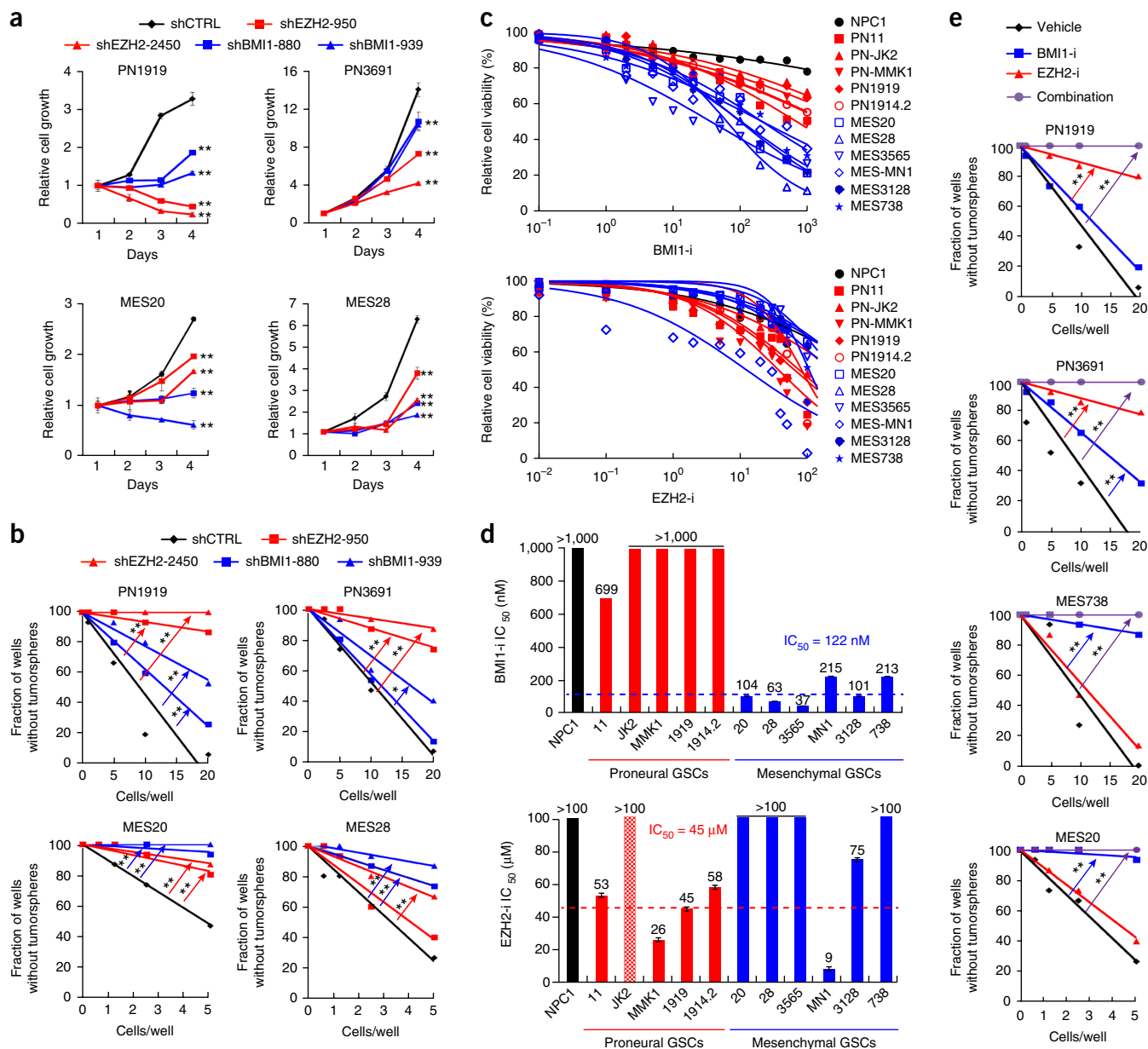
Figure 4 Differential efficacy of BMI1 and EZH2 inhibitors against glioblastoma subgroups. (**a**) Cell growth rates of GSCs transduced with control (shCNTRL), EZH2-specific (shEZH2-950 and shEZH2-2450) or BMI1-specific (shBMI1-880 and shBMI1-939) shRNA ($n = 5$ per group and time point). Data are mean ± s.e.m. **$P < 0.01$, one-way ANOVA with Dunnett's multiple-comparison test. (**b**) *In vitro* limited dilution assay of GSCs transduced with shCNTRL, shEZH2-950 and shEZH2-2450 or shBMI1-880 and shBMI1-939 ($n = 15$ per group). **$P < 0.01$, χ^2 test. (**c**) Cell viability curves of neural progenitors (NPC1), proneural GSCs (PN11, PN-JK2, PN-MMK1, PN1919 and PN1914.2) and mesenchymal GSCs (MES20, MES28, MES3565, MES-MN1, MES3128 and MES738) after treatment with increasing concentrations of BMI1-i or EZH2-i. (**d**) IC$_{50}$ of BMI1-i or EZH2-i for indicated cells. Error bars, mean ± s.e.m. (**e**) *In vitro* limited dilution assay of PN1919, PN3691, MES738 and MES20 cells after treatment with vehicle control, BMI1-i (10 nM), EZH2-i (5 µM) or both ($n = 15$ per group). **$P < 0.01$, χ^2 test.

acetylation of K27 on histone H3 (H3K27ac) on a panel of glioma GSCs and primary patient glioblastoma tissues with proneural or mesenchymal signatures were then compared to results deposited for other gliomas and normal brain. CD44 showed preferential activation, measured by H3K27ac deposition, in mesenchymal models, whereas OLIG2 was more specific for proneural tumors (**Supplementary Fig. 10c**). RNF144A transcriptional regulation was stronger in proneural models and its promoter also bound SOX2, a proneural marker (**Supplementary Fig. 10c**). Supporting a negative regulatory role of RNF144A on BMI1 protein levels, mesenchymal

GSCs showed lower expression of RNF144A protein than normal neural precursors and proneural GSCs (**Supplementary Fig. 10d**). Immunoprecipitation confirmed direct binding of RNF144A to BMI1 (**Supplementary Fig. 10e**). Depleting RNF144A in proneural GSCs with low baseline levels of BMI1 reduced polyubiquitinated BMI1 after proteolysis inhibition and concordantly increased nonubiquitinated BMI1 protein expression (**Fig. 3f**). Nonubiquitinated BMI1 protein in cells in which RNF144A was knocked down by small hairpin RNA (shRNA) persisted at similar levels with or without proteolysis inhibition (**Supplementary Fig. 10f**), highlighting
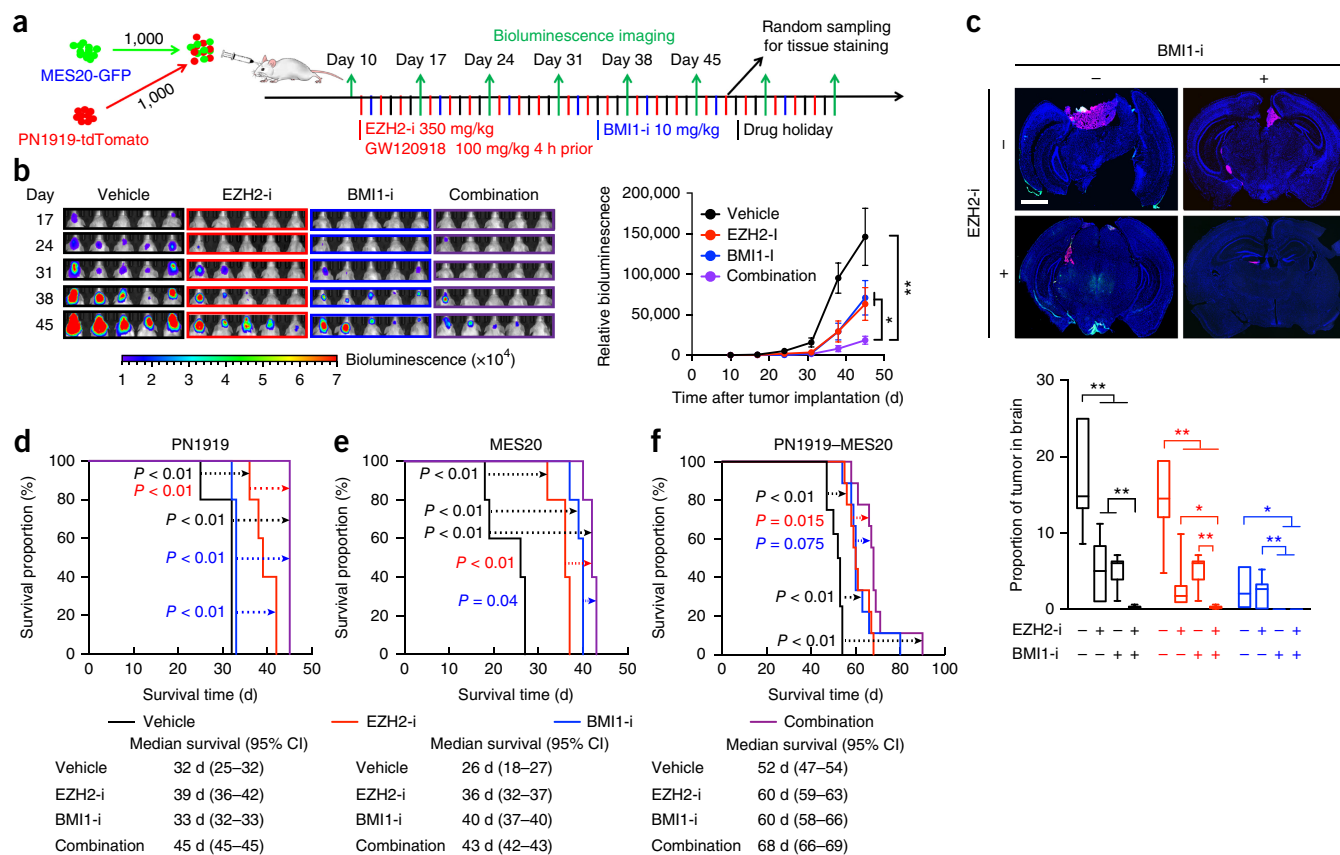
Figure 5 *In vivo* therapeutic efficacy of combined pharmacological inhibition of BMI1 and EZH2 on subtype-mixed glioblastoma model. (**a**) Experimental design to assess *in vivo* effects of BMI1-i (PTC596) and EZH2-i (EPZ6438) on xenograft of mixed proneural (PN1919-tdTomato) and mesenchymal (MES20-GFP) GSCs. (**b**) Left, bioluminescence images of mice bearing mixed proneural and mesenchymal xenografts derived from luciferase-expressing PN1919 and MES20 cells, showing the effect of combined treatment of 10 mg/kg BMI1-i once per week and 350 mg/kg EZH2-i thrice weekly on tumor growth. Time points indicate days after intracranial injection of mixed GSC populations; bioluminescence is measured in photons/s/cm^2/sr. Right, quantification of bioluminescence signals during 45 d of treatment in mice implanted with luciferase-expressing PN1919 and MES20 cells. Signals were normalized to day 10 signaling intensity for each mouse ($n = 10$ per group and time point). *$P < 0.05$; **$P < 0.01$, one-way ANOVA with Tukey's method for multiple comparisons. (**c**) Left, whole-brain images showing distribution of PN1919 (red) and MES20 (green) population in the intermediate tumor samples (day 48). Right, quantification of relative area of occupied by PN1919 (red) and MES20 (green) and total tumor population in the intermediate tumor samples. Vehicle control, $n = 10$; EZH2-i alone, $n = 15$; BMI1-i alone, $n = 14$; combined treatment, $n = 10$. *$P < 0.01$; **$P < 0.01$, one-way ANOVA with Tukey's method for multiple comparisons. Scale bars, 4 mm. (**d,e**) Kaplan–Meier survival curves for mice bearing PN1919 (**d**) or MES20 (**e**) orthotopic tumors with combined treatment of 12.5 mg/kg BMI1-i and 350 mg/kg EZH2-i ($n = 5$ per group). P values were determined by log-rank test. (**f**) Kaplan–Meier survival curves for mice bearing subtype-mixed orthotopic tumors (PN1919 and MES20) after combined treatment of 10 mg/kg BMI1-i once per week and 350 mg/kg EZH2-i thrice weekly ($n = 8$ per group). P values in **e** and **f** were determined by log-rank test.

RNF144A-mediated polyubiquitination as a regulatory node for BMI1 protein degradation.

To determine the clinical relevance of RNF144A in gliomas, we examined its regulation and survival in patient tissues and databases. RNF144A expression was lower in glioblastoma than low-grade glioma (LGG) and inversely related to patient survival (**Supplementary Fig. 11a–d**). Using the LGG–glioblastoma TCGA data set, we mapped the expression of *RNF144A* and *EZH2* mRNA against tumor histology, grade and common molecular features (*IDH1* or *ATRX* mutations; chromosome 1p and 19q co-deletion) as well as patient survival (**Supplementary Fig. 12a**). *RNF144A* mRNA expression showed a strong inverse correlation with glioblastoma histology and *IDH1* mutation and a weaker association with chromosome 1p and 19q co-deletion. Tumors with low *RNF144A* and high *EZH2* mRNA expression (*RNF144A*^{low}*EZH2*^{high}) were enriched with unfavorable microenvironmental transcriptional signatures (**Supplementary Fig. 12b**). To determine the prognostic significance of *RNF144A* and *EZH2* mRNA

levels, we mapped expression levels for each targets and derived survival trends, which showed that *RNF144A*^{low}*EZH2*^{high} tumors had the lowest survival (**Supplementary Fig. 12c**). Multivariate analysis considering patient age, tumor grade and *IDH* mutation status revealed *RNF144A* mRNA and BMI1 activation signatures as independent prognostic factors for overall survival across all grades of glioma (**Supplementary Table 2**) but not glioblastoma (**Supplementary Table 3**). Collectively, these results show that suppression of RNF144A is associated with tumor grade and patient outcome, supporting a negative role in tumor malignancy.

To determine a functional role for differential PRC utilization by GSCs, we examined EZH2 and BMI1 expression in GSCs and neural precursors under stressful conditions, including hypoxia and nutrient restriction. Neural precursors and proneural GSCs lost BMI1 and EZH2 expression, with loss of proneural GSC markers (**Fig. 3g**). In contrast, mesenchymal GSCs under stress showed no changes in BMI1 expression and increases in expression of mesenchymal markers

(**Fig. 3g**). Some mesenchymal GSCs remained viable under stress, whereas almost all neural precursors and proneural GSCs died (**Fig. 3h**). Thus, stress conditions similar to those found in the pseudopalisading necrotic regions may select for mesenchymal glioma cells expressing BMI1 protein. Under low stress, RNF144A depletion in proneural GSCs increased BMI1 expression but did not alter cell proliferation or self-renewal, suggesting that BMI1 is not essential in the absence of stress (**Supplementary Fig. 13a,b**). In contrast, targeting RNF144A expression in proneural GSCs under stress increased cell survival (**Supplementary Fig. 13c**). To further assess PRC function under stress, we depleted either EZH2 or BMI1 using two nonoverlapping specific shRNAs for each target in two proneural and two mesenchymal early passage, patient-derived GSC cultures (**Supplementary Fig. 14a,b**). Targeting of BMI1 or EZH2 protein levels and chromatin effects was confirmed by immunoblot, measured by their respective modifications (H2K119Ub and H3K27me3). BMI1 depletion potently decreased cell viability of mesenchymal GSCs under stress, with modest or no effects on proneural GSCs (**Supplementary Fig. 14c**). In contrast, EZH2 depletion did not sensitize GSCs to harsh growth conditions, suggesting that EZH2 is dispensable under stress. To further support these findings, forced BMI1 expression in proneural GSCs increased cell viability under stress without altering cell growth or tumorsphere formation in the absence of stress (**Supplementary Fig. 14d–g**).

To determine the potential role of BMI1 in mediating *in vivo* tumor growth mimicking regional tumor growth, we performed an *in vivo* cell-mixing experiment with orthotopic co-implantation of BMI1-overexpressing mCherry[+] proneural GSCs and control GFP[+] proneural GSCs (**Supplementary Fig. 14h**). BMI1^{+} cells showed accelerated disease progression, as compared to GFP[+] control proneural GSCs (**Supplementary Fig. 14i**). BMI1-overexpressing cells preferentially localized to CA9^{+} hypoxic regions in the subsequent brain tumors (**Supplementary Fig. 14j**), suggesting that BMI1 confers tumor cell fitness in the hypoxic niche. In line with the preferential expression of EZH2 in proneural cells, RNA interference using two nonoverlapping shRNAs against EZH2 preferentially reduced cell growth and tumorsphere generation of proneural GSCs (**Fig. 4a,b**). Reciprocally, BMI1 depletion preferentially reduced mesenchymal GSC cell growth and tumorsphere formation (**Fig. 4a,b**), demonstrating differential sensitivity to PRC depletion based on molecular subtypes. Collectively, these results support a context-specific role for BMI1, suggesting that differential utilization of PRCs may contribute to divergent subtype-specific niche adaptation and associated poor prognosis.

To leverage our findings for clinical application, we examined the sensitivity of GSC subtypes to PTC596 (BMI1-i), a BMI1 inhibitor, or EPZ6438 (EZH2-i), an EZH2 inhibitor. Mesenchymal GSCs displayed preferential sensitivity to BMI1-i treatment; the half-maximal inhibitory concentration (IC_{50}) of BMI1-i was fourfold lower in mesenchymal GSCs than in proneural GSCs and a neural precursor line (**Fig. 4c,d**), proneural GSCs were generally more sensitive to EZH2-i treatment. Differential sensitivity was confirmed by comparing the mean IC_{50} of BMI1-i and EZH2-i in proneural and mesenchymal GSCs, respectively (**Supplementary Fig. 15a**). To determine combinatorial efficacy, we interrogated the effects of a range of concentrations of each inhibitor against two proneural and two mesenchymal patient-derived GSC cultures (**Supplementary Fig. 15b,c**). While we did not observe a synergistic interaction, the combination of low, clinically achievable concentrations of BMI1 and EZH2 inhibitors completely blocked tumorsphere formation and eradicated GSCs (**Fig. 4e**). As all drugs may have off-target effects, we validated the subtype-specific effect of BMI1 and EZH2 inhibitors on cell viability and tumorsphere-forming ability with structurally unrelated inhibitors: PTC209 (another BMI1 inhibitor) and DZNep (another EZH2 inhibitor) (**Supplementary Fig. 16**).

Systemically delivered drugs against brain tumors must achieve intracranial delivery, as even contrast-enhancing gliomas, representing a disrupted blood–tumor barrier, usually have regions of tumor protected by a barrier. To augment the brain penetration of the EZH2-i, we leveraged a previously developed approach using a combination with the dual ABCCB1 and ABCG2 inhibitor GW120918 (Elacridar)[33]. Measurement of the plasma and brain levels of BMI1-i after treatment indicated that at least 20% of the BMI1-i in blood penetrates into the brain (**Supplementary Fig. 17a,b**). To determine whether the concentrations achievable in the brain were efficacious, we plotted the concentrations of BMI1 and EZH2 inhibitors (PTC596 and EPZ6438, respectively) measured in the brain against the combinational efficacy studies on four different subtype GSCs, consistent with an 80% *in vitro* inhibitory concentration[33] (**Supplementary Figs. 16d** and **17a,b**). Pharmacodynamics analysis of PTC596 and EPZ6438 against intracranial models over a time course confirmed that BMI1 and EZH2 inhibitors specifically attenuated H2K119Ub and H3K27me3 in tumor tissues obtained from orthotopic tumors (**Supplementary Fig. 17c–e**).

Leveraging evidence that the BMI1 and EZH2 inhibitors penetrate into the brain, we examined the therapeutic effects of PTC596 and EPZ6438 on mice bearing intracranial tumors derived from proneural GSCs, mesenchymal GSCs or a mixture of both (**Fig. 5a** and **Supplementary Fig. 18a**). Though the bioluminescent signal was near the limit of detection, bioluminescence imaging confirmed that antitumor effects of EZH2 inhibition were more effective against proneural cells than mesenchymal cells, whereas BMI1 inhibition showed the opposite effect, with combined therapy being more effective (**Fig. 5b** and **Supplementary Figs. 18b–e** and **19**). To address the *in vivo* cellular effects of the EZH2 or BMI1 inhibitor treatments, we xenografted a combination of mCherry[+] proneural and GFP[+] mesenchymal GSCs, treated with vehicle control or the inhibitors (alone or in combination), and analyzed the tumors (**Supplementary Fig. 20**). In mCherry^{+} proneural cells, EZH2-i treatment specifically reduced the number of cells with the PRC2 mark H3K27me3, the GSC marker CD15 and the cell proliferation marker Ki67, whereas mesenchymal cells showed much more modest changes. In contrast, BMI1-i treatment ablated the mesenchymal population. The combination of the BMI1 and EZH2 inhibitors had effects on each marker in both compartments. Cell apoptosis, as measured by active caspase-3, and senescence, as measured by senescence-associated β-galactosidase, did not show substantial changes with any of the therapies tested. Further, we quantified the residual number of each fluorescently labeled tumor cell population after each therapy, confirming preferential activity of each inhibitor of the specific tumor subtype and superiority of combined treatment (**Fig. 5c**). These *in vivo* results translated into superior survival with combined treatment (**Fig. 5d–f**), indicating that the combinatorial inhibition of BMI1 and EZH2 is an effective treatment strategy for heterogeneous microenvironment-dependent subtype glioblastoma.

DISCUSSION

Tumor cell heterogeneity arises from variation in genetics, epigenetic cell state and microenvironment. Single-cell RNA-seq of gliomas demonstrated intratumoral variation in transcription profiles with a fraction of proliferating cells that express stem cell programs[13].

Multiple GSC clones can be derived from a single patient[14,34,35]. Our results refine these observations by linking spatially defined, radiographic features to GSCs with specific transcriptional signatures and response to targeted therapies. We recently reported that mesenchymal GSCs show DNA hypomethylation associated with reduced availability of methionine and hypoxic induction of methyltransferases that deplete methyl donors[36], suggesting that regional epigenetic regulation could extend to DNA methylation. Here we find that stress responses may select for different dependencies on PRCs, with BMI1, a core component of PRC1, promoting cellular survival in areas of low oxygen and nutrient availability. Collectively, these findings support a model in which hypoxia promotes the survival of mesenchymal GSCs by repressing expression of a BMI1 E3 ligase, RNF144A, which results in an increase of BMI1 protein stability. Like neural stem cells, GSCs receive maintenance cues from their microenvironment, but rather than being passive recipients of these cues, they actively remodel their environment through induction of angiogenesis and other features[37]. As we and others have found that hypoxia, acidic stress and nutrient restriction promote GSC maintenance, the RNF144A–BMI1 regulatory mechanism may empower GSCs to reside in stressful microenvironments.

The significance of epigenetic diversity in tumors is supported by genetic observations that 40% of glioblastomas harbor mutations in epigenetic regulators, including BMI1 and EZH2 (ref. 38). Epigenetic dysregulation may induce neoplasia and be amenable to therapeutic targeting, but likely does not adhere to a simple dichotomization of mutations into oncogenes and tumor suppressors, rather permitting cellular plasticity to accelerate tumor evolution. *IDH1* mutations transform astrocytes through modulation of DNA methylation[39]. Mutant IDH1 inhibitors attenuate tumor growth of gliomas harboring *IDH1* mutations[40]. Pediatric glioblastomas are commonly driven by mutations in variant histones, which lead to alterations in DNA methylation and transformation[41–43]. Epigenetic regulators may be particularly effective targets, as oncogenic pathways converge on the epigenome to maintain neoplasia[44]. BMI1 regulates tumor initiation and growth in a genetically engineered murine model of glioblastoma and human stem-like glioma lines[45–48]. BMI1 binds and regulates the promoters of numerous genes, including TGF-β, which has been strongly linked to a mesenchymal phenotype[49]. Targeted therapies against BMI1 have shown preclinical efficacy in a number of cancer types, with effects against cancer stem cells[50]. EZH2 has also been investigated as a cancer therapeutic target, with numerous studies suggesting potential therapeutic benefit against adult and pediatric high-grade gliomas[51–56]. The dynamic interchange of elements between PRC1 and PRC2 suggests that the roles of BMI1 and EZH2 are not biochemically interchangeable but may permit plasticity of cell state under different microenvironmental conditions. Our results support a model in which GSCs are present in different niches with differential utilization of BMI1 and EZH2 (**Supplementary Fig. 21**). Thus, differential region-specific dependency on epigenetic modifiers may inform the development of a combinatorial treatment approach that could collapse intratumoral heterogeneity and limit adaptation to cancer therapeutics.

Little is known about RNF144A beyond its enzymatic function. RNF144A is an E3 ligase for DNA-PKcs[33]. Interrogation of the cBio Portal database shows that several cancer types have *RNF144A* mutations or amplifications, including prostate, breast, uterine and lung (data not shown). One patient with low-grade glioma had a missense mutation, and the TCGA glioblastoma data included one patient with a deletion, one with an amplification and one with a nonsense

mutation (data not shown). Prior reports investigating *BMI1* mRNA expression support increased expression in proneural tumors, but our results demonstrate that BMI1 activity does not correlate with *BMI1* mRNA levels and that BMI1 protein levels are higher in mesenchymal tumors than proneural tumors. RNF144A post-translational regulation of BMI1 is a previously unknown mechanism of BMI1 regulation in glioblastoma and reveals a limitation of transcriptional target discovery. Moreover, the clinical relevance of the RNF144A and BMI1 activation signatures inform biomarker development for BMI1 inhibitors.

Our results demonstrate the efficacy of combined inhibition of BMI1 and EZH2, but the efficacy was not absolute. Though monotherapy against either PRC component hindered tumor growth near the limits of detection, combinatorial therapy against both proneural and mesenchymal tumors achieved the most effective tumor control. Glioblastoma cells can undergo molecular subtype transitions under the influence of different tumor microenvironment that may lead to different effects between *in vitro* and *in vivo* experiments by BMI1 and EZH2 inhibitor treatments. It would be interesting to determine how interconversion between different pools of GSCs may support adaptive resistance to targeted therapies. Our findings suggest that epigenetic therapies against heterogeneous tumors are likely to be more effective in combination than alone. Both BMI1 and EZH2 contribute to resistance to radiation and chemotherapy, suggesting that our dual targeting strategy may be useful in combination with conventional therapies[54,57,58]. Similarly to our prognostic findings, the combined expression of BMI1 and EZH2 in bulk tumor may have greater negative prognostic significance than either target alone[59]. As single tumors may contain different pools of GSCs, we advocate considering not only combined targeting of epigenetic processes, which may prevent the plasticity of cell state transitions, but also GSC pools.

METHODS

Methods, including statements of data availability and any associated accession codes and references, are available in the online version of the paper.

Note: Any Supplementary Information and Source Data files are available in the online version of the paper.

1. Wen, P.Y. & Kesari, S. Malignant gliomas in adults. *N. Engl. J. Med.* **359**, 492–507 (2008).
2. Singh, S.K. *et al.* Identification of human brain tumour initiating cells. *Nature* **432**, 396–401 (2004).
3. Galli, R. *et al.* Isolation and characterization of tumorigenic, stem-like neural precursors from human glioblastoma. *Cancer Res.* **64**, 7011–7021 (2004).
4. Jin, X. *et al.* Blockade of EGFR signaling promotes glioma stem-like cell invasiveness by abolishing ID3-mediated inhibition of p27^{KIP1} and MMP3 expression. *Cancer Lett.* **328**, 235–242 (2013).
5. Bao, S. *et al.* Glioma stem cells promote radioresistance by preferential activation of the DNA damage response. *Nature* **444**, 756–760 (2006).
6. Bao, S. *et al.* Stem cell–like glioma cells promote tumor angiogenesis through vascular endothelial growth factor. *Cancer Res.* **66**, 7843–7848 (2006).
7. Li, Z. *et al.* Hypoxia-inducible factors regulate tumorigenic capacity of glioma stem cells. *Cancer Cell* **15**, 501–513 (2009).
8. Calabrese, C. *et al.* A perivascular niche for brain tumor stem cells. *Cancer Cell* **11**, 69–82 (2007).
9. Hjelmeland, A.B. *et al.* Acidic stress promotes a glioma stem cell phenotype. *Cell Death Differ.* **18**, 829–840 (2011).
10. Flavahan, W.A. *et al.* Brain tumor initiating cells adapt to restricted nutrition through preferential glucose uptake. *Nat. Neurosci.* **16**, 1373–1382 (2013).
11. Verhaak, R.G.W. *et al.* Integrated genomic analysis identifies clinically relevant subtypes of glioblastoma characterized by abnormalities in *PDGFRA, IDH1, EGFR,* and *NF1. Cancer Cell* **17**, 98–110 (2010).
12. Oh, Y.T. *et al.* Translational validation of personalized treatment strategy based on genetic characteristics of glioblastoma. *PLoS One* **9**, e103327 (2014).
13. Patel, A.P. *et al.* Single-cell RNA-seq highlights intratumoral heterogeneity in primary glioblastoma. *Science* **344**, 1396–1401 (2014).
14. Meyer, M. *et al.* Single cell–derived clonal analysis of human glioblastoma links functional and genomic heterogeneity. *Proc. Natl. Acad. Sci. USA* **112**, 851–856 (2015).
15. Halliday, J. *et al. In vivo* radiation response of proneural glioma characterized by protective p53 transcriptional program and proneural–mesenchymal shift. *Proc. Natl. Acad. Sci. USA* **111**, 5248–5253 (2014).
16. Bhat, K.P.L. *et al.* Mesenchymal differentiation mediated by NF-κB promotes radiation resistance in glioblastoma. *Cancer Cell* **24**, 331–346 (2013).
17. Mao, P. *et al.* Mesenchymal glioma stem cells are maintained by activated glycolytic metabolism involving aldehyde dehydrogenase 1A3. *Proc. Natl. Acad. Sci. USA* **110**, 8644–8649 (2013).
18. Joo, K.M. *et al.* Patient-specific orthotopic glioblastoma xenograft models recapitulate the histopathology and biology of human glioblastomas *in situ. Cell Rep.* **3**, 260–273 (2013).
19. Hägerstrand, D. *et al.* Identification of a SOX2-dependent subset of tumor- and sphere-forming glioblastoma cells with a distinct tyrosine kinase inhibitor sensitivity profile. *Neuro Oncol.* **13**, 1178–1191 (2011).
20. Park, T.S. *et al.* Vascular progenitors from cord blood–derived iPSC possess augmented capacity for regenerating ischemic retinal vasculature. *Circulation* **129**, 359–372 (2014).
21. Marotta, D. *et al. In vivo* profiling of hypoxic gene expression in gliomas using the hypoxia marker EF5 and laser-capture microdissection. *Cancer Res.* **71**, 779–789 (2011).
22. Gynther, M. *et al.* Large neutral amino acid transporter enables brain drug delivery via prodrugs. *J. Med. Chem.* **51**, 932–936 (2008).
23. Masouyé, I. *et al.* Endothelial cells of the human microvasculature express epidermal fatty acid–binding protein. *Circ. Res.* **81**, 297–303 (1997).
24. Graeber, T.G. *et al.* Hypoxia-mediated selection of cells with diminished apoptotic potential in solid tumours. *Nature* **379**, 88–91 (1996).
25. Begg, A.C., Stewart, F.A. & Vens, C. Strategies to improve radiotherapy with targeted drugs. *Nat. Rev. Cancer* **11**, 239–253 (2011).
26. Tavares, L. *et al.* RYBP–PRC1 complexes mediate H2A ubiquitylation at Polycomb target sites independently of PRC2 and H3K27me3. *Cell* **148**, 664–678 (2012).
27. Son, M.J., Woolard, K., Nam, D.-H., Lee, J. & Fine, H.A. SSEA-1 is an enrichment marker for tumor-initiating cells in human glioblastoma. *Cell Stem Cell* **4**, 440–452 (2009).
28. Wang, H. *et al.* Role of histone H2A ubiquitination in Polycomb silencing. *Nature* **431**, 873–878 (2004).
29. Kamminga, L.M. *et al.* The Polycomb group gene *Ezh2* prevents hematopoietic stem cell exhaustion. *Blood* **107**, 2170–2179 (2006).
30. Douglas, D. *et al.* BMI-1 promotes Ewing sarcoma tumorigenicity independent of *CDKN2A* repression. *Cancer Res.* **68**, 6507–6515 (2008).
31. Lu, C. *et al.* Regulation of tumor angiogenesis by EZH2. *Cancer Cell* **18**, 185–197 (2010).
32. Ho, S.-R., Mahanic, C.S., Lee, Y.-J. & Lin, W.-C. RNF144A, an E3 ubiquitin ligase for DNA-PKcs, promotes apoptosis during DNA damage. *Proc. Natl. Acad. Sci. USA* **111**, E2646–E2655 (2014).
33. Zhang, P. *et al.* ABCB1 and ABCG2 restrict the brain penetration of a panel of novel EZH2-Inhibitors. *Int. J. Cancer* **137**, 2007–2018 (2015).
34. Piccirillo, S.G.M. *et al.* Distinct pools of cancer stem-like cells coexist within human glioblastomas and display different tumorigenicity and independent genomic evolution. *Oncogene* **28**, 1807–1811 (2009).
35. Segerman, A. *et al.* Clonal variation in drug and radiation response among glioma-initiating cells is linked to proneural–mesenchymal transition. *Cell Rep.* **17**, 2994–3009 (2016).
36. Jung, J. *et al.* Nicotinamide metabolism regulates glioblastoma stem cell maintenance. *JCI Insight* **2**, 90019 (2017).
37. Gilbertson, R.J. & Rich, J.N. Making a tumour's bed: glioblastoma stem cells and the vascular niche. *Nat. Rev. Cancer* **7**, 733–736 (2007).
38. Brennan, C.W. *et al.* The somatic genomic landscape of glioblastoma. *Cell* **155**, 462–477 (2013).
39. Turcan, S. *et al. IDH1* mutation is sufficient to establish the glioma hypermethylator phenotype. *Nature* **483**, 479–483 (2012).
40. Rohle, D. *et al.* An inhibitor of mutant IDH1 delays growth and promotes differentiation of glioma cells. *Science* **340**, 626–630 (2013).
41. Chan, K.-M. The histone H3.3K27M mutation in pediatric glioma reprograms H3K27 methylation and gene expression. *Genes Dev.* **27**, 985–990 (2013).
42. Wu, G. *et al.* Somatic histone H3 alterations in pediatric diffuse intrinsic pontine gliomas and non-brainstem glioblastomas. *Nat. Genet.* **44**, 251–253 (2012).
43. Schwartzentruber, J. *et al.* Driver mutations in histone H3.3 and chromatin remodelling genes in paediatric glioblastoma. *Nature* **482**, 226–231 (2012).
44. Mazor, T. *et al.* DNA methylation and somatic mutations converge on the cell cycle and define similar evolutionary histories in brain tumors. *Cancer Cell* **28**, 307–317 (2015).
45. Bruggeman, S.W.M. *et al.* Bmi1 controls tumor development in an Ink4a/Arf-independent manner in a mouse model for glioma. *Cancer Cell* **12**, 328–341 (2007).
46. Abdouh, M. *et al.* BMI1 sustains human glioblastoma multiforme stem cell renewal. *J. Neurosci.* **29**, 8884–8896 (2009).
47. Godlewski, J. *et al.* Targeting of the Bmi-1 oncogene/stem cell renewal factor by microRNA-128 inhibits glioma proliferation and self-renewal. *Cancer Res.* **68**, 9125–9130 (2008).
48. Venugopal, C. *et al.* Bmi1 marks intermediate precursors during differentiation of human brain tumor initiating cells. *Stem Cell Res.* **8**, 141–153 (2012).
49. Gargiulo, G. *et al. In vivo* RNAi screen for BMI1 targets identifies TGF-β/BMP-ER stress pathways as key regulators of neural- and malignant glioma-stem cell homeostasis. *Cancer Cell* **23**, 660–676 (2013).
50. Kreso, A. *et al.* Self-renewal as a therapeutic target in human colorectal cancer. *Nat. Med.* **20**, 29–36 (2014).
51. Lee, J. *et al.* Epigenetic-mediated dysfunction of the bone morphogenetic protein pathway inhibits differentiation of glioblastoma-initiating cells. *Cancer Cell* **13**, 69–80 (2008).
52. Suvà, M.-L. *et al.* EZH2 is essential for glioblastoma cancer stem cell maintenance. *Cancer Res.* **69**, 9211–9218 (2009).
53. Kim, E. *et al.* Phosphorylation of EZH2 activates STAT3 signaling via STAT3 methylation and promotes tumorigenicity of glioblastoma stem-like cells. *Cancer Cell* **23**, 839–852 (2013).
54. Fan, T.-Y. *et al.* Inhibition of EZH2 reverses chemotherapeutic drug TMZ chemosensitivity in glioblastoma. *Int. J. Clin. Exp. Pathol.* **7**, 6662–6670 (2014).
55. Mohammad, F. *et al.* EZH2 is a potential therapeutic target for H3K27M-mutant pediatric gliomas. *Nat. Med.* **23**, 483–492 (2017).
56. Piunti, A. *et al.* Therapeutic targeting of Polycomb and BET bromodomain proteins in diffuse intrinsic pontine gliomas. *Nat. Med.* **23**, 493–500 (2017).
57. Facchino, S., Abdouh, M., Chatoo, W. & Bernier, G. BMI1 confers radioresistance to normal and cancerous neural stem cells through recruitment of the DNA damage response machinery. *J. Neurosci.* **30**, 10096–10111 (2010).
58. Wu, Z. *et al.* Combined aberrant expression of Bmi1 and EZH2 is predictive of poor prognosis in glioma patients. *J. Neurol. Sci.* **335**, 191–196 (2013).
59. Wang, Q. *et al.* Tumor evolution of glioma intrinsic gene expression subtype associates with immunological changes in the microenvironment. Preprint at *bioRxiv* http://dx.doi.org/10.1101/052076 (2016).

ONLINE METHODS

Human glioblastoma specimens. Excess tumor tissues were collected from glioblastoma patients from whom informed consent was obtained in accordance with approved Institutional Review Board protocols from Cleveland Clinic, Duke University, or University Hospitals-Cleveland Medical Center (UH-CMC). At UH-CMC, the surgeon selected only tumors with significant quantities of enhancing tumor; peritumor regions, which were non-enhancing on T1 weighted MRI with gadolinium but hyperintense on FLAIR imaging and thought to contain infiltrating tumor cells; and necrotic avascular regions in the center of the tumor (enhancing region, enhancing margin, and necrotic region respectively as indicated in **Fig. 1**). Prior to surgery, the surgeon obtained volumetric imaging of the patient and pre-selected distinct areas of enhancing, necrotic and invading tissue to sample according to his surgical strategy. In the operating room, after co-registration was confirmed to be accurate (BrainLab Stealth), the surgeon then sampled regions from these distinct areas using stereotactic techniques at the beginning of the procedure. These distinct specimens from different anatomic regions of each tumor were then processed separately and analyzed as indicated below.

Cells and culture condition. Fresh CD15⁺ GSCs from CW2451, CW2472, and CW2473 glioblastoma primary specimens were isolated with magnetic columns (MACS, CD15 microbeads, Miltenyi Biotec, 130-046-601), and their self-renewal ability, functionally validated by limited dilution assay (LDA). Cultures enriched or depleted for GSCs (PN1919, PN3691, PN1914.2, MES3565, MES738, and MES3128) were isolated from surgical specimens or xenografts and functionally validated as previously described[5–7]. Functional assays included prospective enrichment of stem cell marker expression, sphere formation, and *in vivo* tumor formation. Cellular contamination was ruled out by serial short tandem repeat (STR) analysis and mycoplasma testing. Molecular subtyping was performed by either expression array or RNA sequencing. Normal neural progenitor cells (NPC1 (NHP1), NPC2 (NPC16357), and NPC3 (NPC17893)) and GSCs were maintained in neurobasal medium with B27 (without vitamin A, Invitrogen), basic fibroblast growth factor (20 ng/ml) and epidermal growth factor (20 ng/ml).

Quantitative RT-PCR. Total RNA was isolated with the RNeasy kit (Qiagen) and reverse-transcribed into cDNA using the aScript cDNA SuperMix (Quanta Biosciences). Real-time PCR was performed on an Applied Biosystems 7900HT cycler using SYBR-green Mastermix (SA Biosciences). Expression values were normalized to *18S*. Gene-specific primers as follows: *18S* forward 5′-TGCATGGCCGTTCTTAGTTG-3′ and reverse 5′- AGTTAGCATGCCAGAGTCTC-3′; *DLL3* forward 5′-CCT GCGCGCTGAATGTC-3′ and reverse 5′-CATCGAAACCTGGAGAGA GG-3′; *OLIG2* forward 5′-CTGGCGTCCGAGTCCAT-3′ and reverse 5′-CCTGAGGCTTTTCGGAGC-3′; *ASCL1* forward 5′-CAACGCCA CTGACAAGAAAG-3′ and reverse 5′-GGAGCTTCTCGACTTCACCA-3′; *CD133* forward 5′-TTTTGGATTCATATGCCTTCTGT-3′ and reverse 5′-ACCCATTGGCATTCTCTTTG-3′; *FOXO3* forward 5′-GGTGAATT TCCAATCATCAGC-3′ and reverse 5′-CGAGCTATAGACACCCTG AATG-3′; *MBP* forward 5′-AGGTCTCGTTCCGTGCTG-3′ and reverse 5′-GCCACCATCCCTTGTGAG-3′; *GABRB2* forward 5′- GGAACAATA CTACCTAAGGACAA-3′ and reverse 5′-AGTTTGCAACTTAAATCTC AGTT-3′; *PDGFA* forward 5′-GACCGATCCTCAAGCATCTC-3′ and reverse 5′-AAGGACAAGCGGACAAAATG-3′; *NES* forward 5′- GCAGCAG GAAATATGGGAAG-3′ and reverse 5′-TCTCATGGCTCTGGTTTTCC-3′; *EGFR* forward 5′-CTCCGTTTCTTCTTTGCCCAG-3′ and reverse 5′-GCA CAAGCCACAAGTGTTCC-3′; *AKT2* forward 5′-ACATCATCTCGTA CATGACCAC-3′ and reverse 5′-CTCTGCAAAGAGGGCATCAG-3′; *CD44* forward 5′-TGACACTGTCCAAAGGTTTTC-3′ and reverse 5′-TCA CTAATAGGGCCAGCCTC-3′; *YKL40* forward 5′-CCAAGGAGCCAA ACATCCTA-3′ and reverse 5′-GAAGGGGAAGTAGGATAGGGG-3′; *TIMP1* forward 5′-TGGTAACTCTTTATTTCATTGTCCG-3′ and reverse 5′-CTGAAAAGGGCTTCCAGTCC-3′; and *TGFβ1* forward 5′-GCCAGATCCTGTCCAAGCTG-3′ and reverse 5′-GGTGACCTCCT TGGCGTAGTA-3′; *CA9* forward 5′-ACCTGGTGACTCTCGGCTA CAG-3′ and reverse 5′-CAGCCAGGCAGGAATTCAGC-3′; *GLUT3*

forward 5′-AGCTCTCTGGGATCAATGCTGTGT-3′ and reverse 5′-ATGGTGGCATAGATGGGCTCTTGA-3′; *GLUT1* forward 5′-TCATCGTGGCTGA ACTCTTC-3′ and reverse 5′-GATGAAGACGTAGGGACCAC-3′; *HIF1α* forward 5′-CCTATGTAGTTGTGGAAGTTTTGC-3′ and reverse 5′-ACTA GGCAATTTTGCTAAGAATG-3′; *MCT1* forward 5′-TGTAATCTACCAGTG GTGCTC-3′ and reverse 5′-AACCTACTTCTTTCCCCCATC-3′; *MCT4* forward 5′-GGGTCATCACTGGCTTGGGT-3′ and reverse 5′-GGAACACGGGACTG CCTGC-3′; *LDH5* forward 5′-TGCTGTACGTACTGCATTTGC-3′ and reverse 5′-ATCCCAGGATGTGACTCACTG-3′; *CD31* forward 5′-AAGGCCA GATGCACATCC-3′ and reverse 5′-TTCTACCCAACATTAACTTAGCAGG-3′; *VEGFR2* forward 5′-TAGCATGTCTTATAGTCATT-3′ and reverse 5′-CACT CTCTGAATGATTATTA-3′; *CD34* forward 5′-CCGTCATTGAAACCAGG-3′ and reverse 5′-TCATAGCCCAGATCAGCTC-3′; *ACTIN* forward 5′-AGAAAT CTGGCACCACACC-3′ and reverse 5′- AGAGGCGTACAGGGATAGCA-3′; *VEGFB* forward 5′-CCATCTCTTTTATCAGGGTTGG-3′ and reverse 5′-CTCTG TGCAAGTAAGCATCTTACA-3′.

Western blot analysis and immunoprecipitation assay. Cells were collected and lysed in IP Lysis buffer (Thermo Scientific) containing phosSTOP phosphatase inhibitor cocktail (Roche) and protease inhibitor cocktail (Sigma) and separated by 12% SDS–PAGE (NuPAGE Bis-Tris gel, Invitrogen) and transferred to PVDF membranes (Millipore). Membranes were blocked with 5% (wt/vol) nonfat milk in PBS + Tween-20 (0.5% vol/vol) and probed with primary antibodies against BMI1 (1:1,000, Abcam, ab126783), H2K119Ub (1:1,000, Cell signaling, #8240S), CD44 (1:1,000, BD Biosciences, 550392), YKL40 (1:1,000, Abcam, ab86428), EZH2 (1:1,000, BD Biosciences, 612667), H3K27Me3 (1:1,000, Millipore, 07-689), OLIG2 (1:1,000, R&D system, AF2418), SOX2 (1:1,000, R&D system, AF2018), RNF144A (1:500, Abcam, ab89260), Ub (1:5,000, Santa Cruz, sc-9133), tubulin (α-tubulin,1:10,000, Sigma-Aldrich, T6074), and ACTIN (β-actin,1:10,000, Sigma-Aldrich, A1978). BMI1-RNF144A interaction and BMI1 polyubiquitination were detected by Pierce Crosslink magnetic IP and Co-IP kit (Thermo Scientific). For the ubiquitination assays, cells were treated with Lactacystin (5 μM or 10 μM; Sigma) for 5 h before collection. BMI1 polyubiquitination was quantified by ImageJ.

Immunofluorescence and β-gal staining. 10-μm thick slides of deidentified frozen multiregional samples (glioblastoma patient CW1757 according T1-weighted MRI images) and PN3691 (VEC/BMI1) xenografted frozen brain tissue were fixed in 4% paraformaldehyde and immunolabeled using primary antibodies to SOX2 (1:500, R&D system, AF2018), CD44 (1:100, BD Biosciences, 550392), vWF (1:500, Millipore, AB7356), CA9 (1:100, Genetex, GTX70020), H3K27me3 (1:1,000, Millipore, 07-689), H2AK119Ub (1:500, Cell Signaling, 8240S), CD15 (1:100, Millipore, MAB4301), Ki67 (1:100, Dako, M7240), active CASPASE3 (1:100, Cell Signaling, 9661S) and the secondary fluorescence-labeled antibodies. Nuclei were counterstained with DAPI. Immunofluorescence images were taken by a Leica TCS SP5 Confocal Microscope or a Leica SCN400 Slide Scanner. A senescence β-galactosidase staining kit (Cell Signaling, 9860S) was used to detect senescent cells in tumor tissues, the phase-contrast light images were captured by Leica DM4000 B microscope.

Tissue microarray (TMA) and immunohistochemistry. 5-μm thick slides of deidentified paraffin-embedded tissue microarrays (TMAs) were constructed from glioma after obtaining Ohio State University Institutional Review Board Approval. A total of 96 cases were arrayed on the TMA block, including 15 non-neoplastic controls (cortical dysplasias), 16 grade II glioma cases, 27 grade III gliomas, and 38 grade IV glioblastomas. Tissues too small and/or crushed on the TMA were eliminated from analysis after immunohistochemistry staining with anti-BMI1 (1:50, Abcam, ab126783), anti-EZH2 (1:100, BD Biosciences, 612667), anti-CD44 (1:100, BD Biosciences, 550392), anti-OLIG2 (1:100, R&D system, AF2418), and secondary HRP-conjugated antibodies. The TMA images were taken by a Leica SCN400 Slide Scanner. Overall staining on TMA was scored as negative (−) or positive (+) compared to non-neoplastic controls. PN3691 (with or without treatment with BMI1 or EZH2 inhibitors) xenografted brain tissues were fixed in 4% PFA and stained with anti-H2K119Ub (1:100, Cell Signaling, 8240S), anti-H3K27me3 (1:1,000, Millipore, 07-689), and secondary HRP-conjugated antibodies. Nuclei in

immunohistochemistry were counterstained with hematoxylin. The immunohistochemistry images were taken by a Leica DM4000B Microscope, and were analyzed by IHC Profiler.

Cell viability and growth assays. Cell viability was measured by CellTiter-Glo Luminescent Cell Viability Assay (Promega) according to the manufacturer's instructions after exposing 3 d under different conditions including low-glucose (0.45 g/l glucose)[10], hypoxia (1% oxygen)[7], BMI1 inhibitor (PTC596, PTC therapeutics; PTC209, PTC therapeutics), and EZH2 inhibitor (EPZ6438, Medchemexpress LLC; DZNep, SELLECKCHEM). 1×10^6 cells were seeded for cell viability under low-glucose or/and hypoxic conditions, 2×10^3 cells were seeded for drug response under BMI1 or EZH2 inhibitor treatment. IC_{50} values of BMI1 or EZH2 inhibitors were calculated with GraphPad Prism software. For competitive response assay of BMI1 and EZH2 inhibitors, the proportion of GFP^+ or $mCherry^+$ cells was determined by flow cytometry after treatment the co-cultured MES83-GFP and PN528-mCherry cells with PTC-209, and DZNep. Two-dimensional titration assay was performed on four different subtype GSCs after combined treatment with different doses of PTC596 and EPZ6438. Relative cell growth was measured over a four-day time course using CellTiter-Glo Luminescent Cell Viability Assay kit (Promega) after seeding 1×10^3 cells.

In vitro **limiting dilution tumorsphere formation assay.** For detection of stem cell frequency change by BMI1 and EZH2 signaling pathway, different numbers of cells per well (range of 40–1 cells per well) were seeded in 96-well plates containing 100 μl completed neurobasal medium with or without BMI1 or/and EZH2 inhibitors, and added 20 μl completed neurobasal medium with or without BMI1 or/and EZH2 inhibitors per 3 d. After 14 d, the tumorspheres were measured and analyzed by Extreme Limiting Dilution analysis software (http://bioinf.wehi.edu.au/software/elda).

Plasmid and lentiviral or retroviral transduction. Lentiviral plasmids for targeting EZH2 (TRCN0000040077 for shEZH2-950, and TRCN0000293738 for shEZH2-2450), BMI1 (TRCN0000020158 for swhBMI1-880, and TRCN0000020157 for shBMI1-939), RNF144A (TRCN0000004414 for shRNF144A-1099, and TRCN0000004416 for shRNF144A-3112) and nonspecific control sequence (SCH002 for shCNTRL) were purchased from Sigma-Aldrich. Lentiviral plasmids pGIPZ-GFP, PRSC-mCherry, L-2-G, and L-2-T were used to label the BTIC cells in *in vivo* experiments. Lentiviral particles were produced in 293T cells with PAX2 and PMD2G helper plasmids (Addgene) in stem cell medium. Retroviral plasmids PMSC-BMI1 and PMSC-VEC (control) were used to produce retroviral particles in 293T cells with pCMV-VSVG and pCMV-Gag-Pol helper plasmids (Addgene).

Calculation of achievable drug concentrations. Zhang and co-workers reported the pharmacokinetics of the EZH2 inhibitor, EPZ6438, in combination with the ABCB1 and ABCG2 inhibitor, GW120918 (Elacridar)[33]. They found that the EPZ6438 concentration was 1.5 μg/ml in the plasma and 0.35 mg/kg in the brain 1 h after treatment with 2.5 mg/kg EPZ6438 and 100 mg/kg GW120918. On the basis of these observations and the likely contamination of the brain measurements by blood, we calculated the minimum brain concentration as $(1.5 \times 0.35)/2.5 = 0.21$ μg/ml. Our studies used 350 mg/kg of EPZ6438 (for example, 140-fold higher dose), leading to a calculated brain concentration of 29–210 μg/ml. The molecular weight of EPZ6438 is 572.74, translating into a calculated brain concentration range of 51–366 μM. We determined the concentration of the BMI1 inhibitor 4 h after combined treatment with 10 mg/kg or 12.5 mg/kg BMI1 inhibitor PTC596 (MW 420.34) and 350 mg/kg EZH2 inhibitor EPZ6438 in the plasma and brain. 10 mg/kg BMI1 inhibitor treatment achieved 1 μg/ml in plasma and 2 mg/kg in the brain. Using the same approach that we used for the EZH2 inhibitor concentration calculations, we estimated the brain concentration range of the BMI1 inhibitor administered at 10 mg/kg as 475.8–2,379 nM. Collectively, *in vivo* drug ranges for each agent achieved concentrations consistent with those we detected as having combinational benefit in IC80 concentrations from two-dimensional drug concentration assays (51.3–366.7 μM for the EZH2 inhibitor and 158.6–793 nM (1/3 of 475.8–2,379 nM) for the BMI1 inhibitor).

Animal experiments. All animal studies were performed in accordance with Cleveland Clinic IACUC approved protocols. Required sample sizes were calculated by an a priori power analysis. All mice were randomly assigned to appropriate treatment groups. For the co-implantation study, 2.5×10^5 PN3691-mCherry-BMI1 and 2.5×10^5 PN3691-GFP-VEC cells (BMI1/VEC), or 5×10^5 PN3691-GFP-VEC (VEC/VEC control) cells were implanted into the right frontal lobes of 3-week-old NOD SCID-γ (NSG) mice as previously described[7]. For pharmacokinetic study, BMI1 inhibitor (PTC596) concentration in plasma and brain was determined by HPLC-coupled mass spectrometry after oral administration of BMI1 inhibitor (PTC596) or EZH2 inhibitor (EPZ6438) with GW120918 (dual ABCCB1 and ABCG2 inhibitor; Medchemexpress LCC) to enhance EPZ6438 uptake into brain[33]. For pharmacodynamic testing of BMI1 and EZH2 inhibitors, 5×10^5 PN3691 cells were implanted intracranially into NSG mice. After 1 week, the BMI1 inhibitor (PTC596) or EZH2 inhibitor (EPZ6438) with GW120918 were administered orally by gavage. For testing, *in vivo* inhibition effect of BMI1 and EZH2 inhibitors, 1×10^5 luciferase-expressing PN1919 or MES20 cells for single subtype glioblastoma model, and 1,000 RFP-labeled PN1919 and 1,000 GFP-labeled MES20 cells for subtype-mixed glioblastoma model were implanted intracranially into NSG mice. When the luciferase signals from tumor cells were detectable (after 4 d for single subtype model, and 10 d for subtype-mixed model), the BMI1 inhibitor or EZH2 inhibitor with GW120918 were administered orally by gavage. The size of orthotopic tumor was monitored by bioluminescence channel of IVIS Spectrum. The investigators were blinded to the group allocation and study outcome assessments of all mice.

Chromatin immunoprecipitation (ChIP) assay. ChIP of 5–10 mg of flash-frozen primary glioblastoma tumors and 1 million fresh $CD15^+$ GSCs was performed using H3K27Ac (5 mg; Active Motif, 39133), H3K27me3 (5 mg; Active Motif, 39155), and H2AK119Ub (10 mg, Cell Signaling, #8240S) antibodies per ChIP experiment (Abcam, AB4729). Enriched DNA was quantified using Picogreen (Invitrogen) and ChIP libraries were amplified and barcoded using the Thruplex DNA-seq library preparation kit (Rubicon Genomics) according to manufacturer recommendations. Following library amplification, DNA fragments were agarose gel (1.0%) size selected (<1 kb), assessed using Bioanalyzer (Agilent Technologies) and sequenced at the Center for Applied Genomics (the Hospital for Sick Children) using Illumina HiSeq 2000 100-bp single-end sequencing. Sequencing reads were aligned using Bowtie2 to the hg19 (http://hgdownload.cse.ucsc.edu/) genome using default settings. HOMER was used for calling peaks in the H3K27me3 and H2AK119ub data sets versus ChIP input data with the following settings: -F 2, -P 0.01, -L 2, -LP 0.01, -minDist 5000 –size 1000. Region-specific peaks were identified using the BEDTools subtract function and overlapping peaks were defined using the BEDtools intersect function. Gene Ontology Pathway analysis was performed using the gene-set enrichment analysis (GSEA) molecular signatures database at http://software.broadinstitute.org/gsea/index.jsp and using the HOMER annotatePeaks function. Molecular Signature bubble plots were created using Cytoscape v3.5 and the Bader Lab Enrichment Map software (http://www.baderlab.org/Software/EnrichmentMap).

RNA sequencing. Total RNA was extracted with TRIzol (Invitrogen), separated using Phase Lock Gel tubes (5 Prime), and purified using the miRNAeasy kit (Qiagen). Total RNA was prepared for sequencing by Beckman-Coulter Genomics using the Illumina TruSeq Stranded Total RNA Library Prep Kit. RNA-seq libraries were sequenced on the Illumina HiSeq 2500 platform by Beckman-Coulter Genomics. For gene expression analysis, reads were aligned to the hg19 genome build (retrieved from http://cufflinks.cbcb.umd.edu/igenomes.html) using TopHat v2.0.6. Paired-end 125-bp reads were generated on an Illumina HiSeq 2500 instrument at the Case Western Reserve University Genomics Core Facility. Reads were aligned to the hg19 genome using TopHat v2.0.6 with the library type option set to first strand. FPKM values for known genes were calculated using Cufflinks v2.0.2 provided with the GTF file via the -G (known genes only) option. FPKM values were quantile normalized.

In silico **analyses.** Collected *in silico* resources, including transcript microarray data, RNA-seq, patient survival, and anatomic information of patient samples were downloaded from TCGA (https://tcga-data.nci.nih.gov/docs/publications/tcga/-JC) and Ivy GAP (http://glioblastoma.alleninstitute.org) portal websites.

GBM molecular subtypes (including proneural, classical, and mesenchymal), EZH2 and BMI1 activation or inhibition signatures were informed by previous publications[29,30,59]. Microenvironment-related gene signatures included: mature-vascular signature (MATURE_VAS), nine genes significantly upregulated twofold in human umbilical vein endothelial cells ((HUVEC) compared to human microvascular endothelial cells (HMEC) (**Supplementary Fig. 2a,b**); microvascular signature (MICRO_VAS), eight genes significantly upregulated twofold in HMEC compared to HUVEC (**Supplementary Fig. 2a,b**); hypoxia activation signature (HYPOXIA_AC), nine genes significantly upregulated twofold in hypoxic regions compared to normoxia region (**Supplementary Fig. 3a,b**); hypoxia inhibition signature (HYPOXIA_IN), 23 genes significantly downregulated in hypoxic regions compared to normoxia regions (**Supplementary Fig. 3a,b**). Single-sample GSEA (ssGSEA) was used to analyze gene signature enrichment in TCGA and Ivy GAP data sets. Correlation of genes and signatures was analyzed by Excel, and patient survival was analyzed with GraphPad Prism.

Statistical analysis. All grouped data are presented as mean ± s.e.m. Significance between groups was analyzed by one-way ANOVA or Student's *t*-test using GraphPad Prism. The *F*-values and DF for each ANOVA test can be found in the **Life Sciences Reporting Summary** associated with this manuscript. Correlation coefficients were calculated by Excel. Kaplan–Meier survival curves were generated by GraphPad Prism, and log-rank *P* value was used to determine significance. All experiments were repeated in each specimen presented in at least biological duplicates (patient-derived xenograft cell models) with technical triplicates. Multivariate linear regression was performed using R 3.2.4. Independent variables were tumor type by histology (astrocytoma, oligoastrocytoma, oligodendroglioma, or glioblastoma), *IDH1* mutation status (wild-type versus mutant), chromosome 1p and 19q co-deletion (co-deleted versus not) and *ATRX* status (wild-type versus mutant). Sample size was determined using the appropriate power calculation formula in JMP (Version 12, SAS Institute Inc.) for each experimental setup. This study complies with randomization in grouping age-matched mice into different experimental arms. The investigator was blinded to the group allocation during the experiment and/or when assessing the outcome.

Data availability. All raw ChIP-seq and RNA-seq data are available in the NCBI Gene Expression Omnibus (GEO GSE103366).

natureresearch

Corresponding Author:	Jeremy N. Rich
Date:	August 31, 2017

Life Sciences Reporting Summary

Nature Research wishes to improve the reproducibility of the work we publish. This form is published with all life science papers and is intended to promote consistency and transparency in reporting. All life sciences submissions use this form; while some list items might not apply to an individual manuscript, all fields must be completed for clarity.

For further information on the points included in this form, see Reporting Life Sciences Research. For further information on Nature Research policies, including our data availability policy, see Authors & Referees and the Editorial Policy Checklist.

▸ Experimental design

1. Sample size

   Describe how sample size was determined.

   > The number of animals per arm is based upon the following calculation:
   > $N=1+2C(s/d)^2$ where:
   > N = number of animals per arm
   > C = 7.85 when alpha=0.05 and 1-beta=0.8 (significance level of 5% with a power of 80%)
   > s = standard deviation, and
   > d = difference to be detected.
   > These parameters are derived from prior experience with similar studies, leading to a final sample size of at least 5 animals per arm.

2. Data exclusions

   Describe any data exclusions.

   > No piece of data from experiments presented in this manuscript was excluded.

3. Replication

   Describe whether the experimental findings were reliably reproduced.

   > All experimental findings were repeated using multiple patient-derived models as cell line replicates (biological replicates) with technical replicates in each experiment.

4. Randomization

   Describe how samples/organisms/participants were allocated into experimental groups.

   > All animal experiments underwent randomization at entry. age- and gender-matched mice were randomly allocated to each experimental arm through blinding the experimenter to animals. Animal subjects were randomly assigned to treatment groups and during analysis.

5. Blinding

   Describe whether the investigators were blinded to group allocation during data collection and/or analysis.

   > For bioluminescent imaging experiments of tumor-bearing mice treated with monotherapy or combinatorial therapy, the experimenter was blinded to the mice selected for imaging on IVIS imager.

   Note: all studies involving animals and/or human research participants must disclose whether blinding and randomization were used.

6. Statistical parameters

For all figures and tables that use statistical methods, confirm that the following items are present in relevant figure legends (or the Methods section if additional space is needed).

n/a	Confirmed	
☐	☒	The <u>exact</u> sample size (*n*) for each experimental group/condition, given as a discrete number and unit of measurement (animals, litters, cultures, etc.)
☐	☒	A description of how samples were collected, noting whether measurements were taken from distinct samples or whether the same sample was measured repeatedly.
☐	☒	A statement indicating how many times each experiment was replicated
☐	☒	The statistical test(s) used and whether they are one- or two-sided (note: only common tests should be described solely by name; more complex techniques should be described in the Methods section)
☐	☒	A description of any assumptions or corrections, such as an adjustment for multiple comparisons
☐	☒	The test results (e.g. *p* values) given as exact values whenever possible and with confidence intervals noted
☐	☒	A summary of the descriptive statistics, including central tendency (e.g. median, mean) and variation (e.g. standard deviation, interquartile range)
☐	☒	Clearly defined error bars

See the web collection on statistics for biologists for further resources and guidance.

▶ Software

Policy information about availability of computer code

7. Software

Describe the software used to analyze the data in this study.

> Microsoft Excel, Matlab R2016a, R v3.3.0, GraphPad Prism, HOMER, TopHat2, BedTools, Cufflinks

For all studies, we encourage code deposition in a community repository (e.g. GitHub). Authors must make computer code available to editors and reviewers upon request. The *Nature Methods* guidance for providing algorithms and software for publication may be useful for any submission.

▶ Materials and reagents

Policy information about availability of materials

8. Materials availability

Indicate whether there are restrictions on availability of unique materials or if these materials are only available for distribution by a for-profit company.

> - All cell lines and constructs are available to anyone in the community through appropriate material transfer agreements.
> - BMI1 inhibitors PTC596 and PTC209 are available for distribution through PTC Therapeutics (South Plainfiled, NJ, USA).

9. Antibodies

Describe the antibodies used and how they were validated for use in the system under study (i.e. assay and species).

> BMI1 (Abcam Ab126783)
> H2AK119Ub (Cell Signaling #8240S)
> CD44 (BD Biosciences 550392)
> YKL40 (Abcam ab86428)
> EZH2 (BD Biosciences 612667)
> H3K27Me3 (Western, IF) (Millipore 07-689)
> H3K27Me3 (ChIP) (Active Motif 39155)
> OLIG2 (R&D system AF2418)
> SOX2 (R&D system AF2018)
> RNF144A (Abcam ab89260)
> Ub (Santa Cruz sc-9133)
> TUBULIN (Sigma-Aldrich T6074)
> ACTIN (Sigma-Aldrich A1978)
> vWF (Millipore AB7356)
> CA9 (Genetex GTX70020)
> CD15 (Millipore MAB4301)
> Ki67 (Dako M7240)
> active CASPASE3 (Cell signaling 9661S)
> H3K27ac (Active Motif 39133)

10. Eukaryotic cell lines

    a. State the source of each eukaryotic cell line used.

- All GSC models were derived from disassociation of patient specimens. -293T cells used to produce virus for transduction were obtained from the CCF/LRI cell culture core.

    b. Describe the method of cell line authentication used.

All GSC models were verified for purity using STR analysis.

    c. Report whether the cell lines were tested for mycoplasma contamination.

All cell lines were regularly tested for mycoplasma contamination.

    d. If any of the cell lines used in the paper are listed in the database of commonly misidentified cell lines maintained by ICLAC, provide a scientific rationale for their use.

N/A

▶ Animals and human research participants

Policy information about studies involving animals; when reporting animal research, follow the ARRIVE guidelines

11. Description of research animals

    Provide details on animals and/or animal-derived materials used in the study.

For all animal experiments were performed with 3-4 week-old male and female NSG mice

Policy information about studies involving human research participants

12. Description of human research participants

    Describe the covariate-relevant population characteristics of the human research participants.

All patients whose excess tissue specimens were analyzed in this study were informed and consented according to respective IRB protocols approved by the Cleveland Clinic Foundation, University Hospitals, and The Ohio State University Medical Center.